

Tailored and improved protonic conductivity through Ba(Z_xCe_{10-x})0.08 $Y_{0.2}O_{3-\delta}$ ceramics perovskites type oxides for electrochemical devices

Kwati Leonard*

International Institute for Carbon-Neutral Energy Research (I2CNER), Kyushu University 744 Motooka, Nishi-ku, Fukuoka 819-0395, Japan

E-mail:kwati@i2cner.kyushu-u.ac.jp

Yuji Okuyama,

Research Center for Sustainable Energy and Environmental Engineering, Faculty of Engineering, University of Miyazaki, 1-1 Gakuenkibanadai Nishi, Miyazaki 889-2192, Japan *Mariya E. Ivanova*

Institute of Energy- and Climate Research IEK-1, Forschungszentrum Jülich GmbH, 52425 Jülich Germany

Wilhelm A. Meulenberg

Institute of Energy- and Climate Research IEK-1, Forschungszentrum Jülich GmbH, 52425 Jülich Germany

Hiroshige Matsumoto*

International Institute for Carbon-Neutral Energy Research (I2CNER), Kyushu University 744 Motooka, Nishi-ku, Fukuoka 819-0395, Japan

E-mail:(kwati@i2cner.kyushu-u.ac.jp, matsumoto@i2cner.kyushu-u.ac.jp)

Keywords: (Proton conductor, electrical conductivity, hydration, stability, steam electrolysis)

Abstract

Acceptor-doped barium zirconate cerate electrolytes constitute prospective materials for highly efficient and environmentally friendly electrochemical devices. This manuscript employs a systematic approach to further optimize ionic conductivity in $Ba(Zr_xCe_{10-x})_{0.08}Y_{0.2}O_{3-\delta}$, $(1 \le x \le 9)$ oxides for moderate temperature electrolysis. We found two new composition variants by fixing a cerium/zirconium ratio of 5/4 at the perovskite B-site with incremental zirconium, an observation that contrasts many reports suggesting a linear decrease in conductivity with increasing zirconium. As a result, the composition $BaZr_{0.44}Ce_{0.36}Y_{0.2}O_{3-\delta}$ demonstrates a superior ionic conductivity (10.1 mS cm⁻¹ at 500 °C) to stability trade-off

whereas, BaZr_{0.16}Ce_{0.64}Y_{0.2}O_{3-δ} exhibits the highest conductivity (11.5 mS cm⁻¹ at 500 °C) among the studied pellets. The high protonic conductivity is associated with a high degree of hydration, as confirmed by thermo-gravimetric analysis. In addition, both compositions as electrolytes allow successful hydrogen production in a steam electrolyzer prototype. Electrolysis voltage as low as 1.3 V is attainable at current densities of 600 and 500 mA /cm² respectively at 600 °C, achieving 82 % current efficiencies with the later electrolyte.

1. Introduction

Perovskites type yttrium doped BaZrO₃-BaCeO₃ solid solutions represent some of the most promising electrolyte materials for future intermediate temperature electrochemical devices^[1–4]. They exhibit outstanding conductivity under a humidified hydrogen-containing atmosphere in the 400~700 °C temperature range due to the proton motion within their lattices with lower activation energy^[5–8] than conventional oxygen ion conductors like yttria-stabilized zirconia (YSZ). The proton transport kinetics within the crystal lattices are closely related to oxygen vacancies created due to the B-site substitution of a tetravalent cation with a trivalent dopant (e.g., Y³⁺, Sc³⁺, Yb³⁺)^[5,9,10]. Commonly referred to as acceptor doping in the A²⁺B⁴⁺O₃²⁻ type perovskites^[9,11]. The basicity of the system increases after the substitution, and oxygen vacancies are formed to compensate for charge neutrality. As a result, the material becomes more reactive to water vapor and allows the following hydration reaction:

$$H_2O + V_0^{"} + O_0^{\times} \leftrightarrow 2OH_0^{"}$$
 (1)

where $V_0^{\cdot \cdot}$ is an oxide-ion vacancy, O_0^{\times} is an oxide ion on an oxygen site, and $OH_{\cdot 0}^{\cdot \cdot}$ represents a hydroxyl group formed upon proton incorporation and referred to as a protonic defect^[5,12,13]. The primary underlying mechanisms for the mobility of these defects have been investigated extensively and suggested to involve protons transfer and reorientation of hydroxide ions on the oxygen sites and between neighboring oxygen ions^[9]. Proton concentration in the oxide depends on the partial pressures of water vapor, whereas proton conductivity is the product of

proton concentration and proton diffusivity in the material. In oxidizing conditions, however, electronic defects can compensate for the vacancies via Eq (2), leading to a p-type hole (h') conduction, with the hole concentration proportional to one-fourth power of the partial pressure of the oxygen, typically appearing at high oxygen partial pressure.

$$\frac{1}{2}O_{2(g)} + V_0^{"} \to O_0^x + 2h^{"}.....(2)$$

The choice of dopant that can produce high proton concentration and high proton diffusivity within any desired temperature range is an essential prerequisite for high protonic conductivity in these materials. Based on literature reports, yttrium is the most commonly used acceptor dopant that induces oxygen vacancies^[6,14,15]. In most cases, the conductivity also increases with decreasing electronegativity of A and B site elements^[9]. Besides dopant choice, hydration also plays a crucial role in defining the ionic properties of these materials and strongly impacts device performance.

A wide range of Y_2O_3 doped $BaZrO_3$ - $BaCeO_3$ solid solutions has been studied as candidate fuel cells and electrolyzer electrolyte materials^[2,4,16–18], with significant efforts to understand their chemical and physical properties. A significant challenge, however, has been their chemical stability. Individually Y_2O_3 doped $BaCeO_3$ ceramics show high charge carrier concentration ($\sim 10^{-2}$ to 10^{-1} S cm⁻¹ order at 600 °C) when doped with 15 or 20 % $Y^{[19,20]}$ and a coarser microstructure. However, a key challenge is their chemical stability, especially under H_2O vapor at low temperatures and CO_2 at elevated temperatures^[21,22], posing a significant concern for practical usage and long-term operation. Conversely, $BaZrO_3$ based ceramics provide better chemical stability under high steam content, less parasitic electronic conduction, but limited proton conductivity due to the pronounced blocking effects of the grain boundaries than the cerate counterparts^[23]. Therefore, some studies suggest replacing Ce^{4+} (R=0.87 Å) with ions of different sizes such as and Zr^{4+} (R=0.72 Å) or Nd^{3+} (R=0.983 Å) seems the best choice strategy that combines high conductivity and good chemical stability^[21,24–29]. This

concept was first explored in depth by Wienströer et al., using Nd-doped barium cerate-zirconates (BaCe_{0.9-x}Zr_xNd_{0.1}O_{2.95} for $0.1 \le x \le 0.9$) solid solutions. For most of these studies, the replacement of Ce⁴⁺ adversely affects the conductivity, which interns decreases monotonously with increasing Zr content. For example; Katahira et al. ^[24] and Haile S. M. et al. ^[21] reported a linear dependence of the conductivity of Zr-substituted BaCe_{0.9-x}Zr_xM_{0.1}O_{3-\sigma} perovskites (M = Yb, Gd, Nd) and reinforced chemical stability against CO₂ with incremental zirconium content. Similarly, Murphy R. et al. ^[28] also showed similar conductivity trends with increasing Hf content and improved chemical stability, thus confirming a trade-off between stability and conductivity. Upon modifying the Zr ratio in SrZr_{0.9-x}Ce_xY_{0.1}O_{3-\delta}, Matsumoto et al. ^[29], however, observed a discontinuous change of conductivity with a maximum value (4.6×10⁻³ S cm⁻¹ at 600 °C) at the ratio of Zr to Ce of 5:4, even though the precise reason for the high conductivity is still elusive. In the quest to clarify the origin of the high conductivity in SrZr_{0.5}Ce_{0.4}Y_{0.1}O_{3-\delta}, the present authors and others ^[30-33] have systematically examined this composition to correlate electrical conductivity to the crystal structure and device performance.

In this work, we perform a systematic study to optimize ionic conductivity further in the $Ba(Zr_xCe_{1-x})Y_yO_{3-\delta}$ family and overcome the inherent instability in CO_2 environments of the current state-of-the-art proton conductor. In a previous study, on $SrZr_{0.9-x}Ce_xY_{0.1}O_{3-\delta}$ (x=0-0.9) system, our group identified $SrZr_{0.5}Ce_{0.4}Y_{0.1}O_{3-\delta}$ composition as discussed above, to have the highest electrical conductivity (4.5×10^{-3} S cm⁻¹ at 600 °C) within the series. Starting from this composition ($SrZr_{0.5}Ce_{0.4}Y_{0.1}O_{3-\delta}$), we substituted Ba for Sr in the A-site and increased the Y content from 0.1 to 0.2 mol % while fixing the Zr/Ce ratio constant at 5:4 in the perovskite B-site. As a result, we found two new composition variants, $BaZr_{0.44}Ce_{0.36}Y_{0.2}O_{3-\delta}$, demonstrating a superior ionic conductivity to stability trade-off than the current benchmark proton conductor, reported in many critical proton-conducting electrochemical cell applications. Whereas composition $BaZr_{0.16}Ce_{0.64}Y_{0.2}O_{3-\delta}$ exhibits the highest electrical conductivity among

the studied Ba(Zr_xCe_{10-x})_{0.08}Y_{0.2}O_{3- δ} pellets. The high protonic conductivity for both specimens is also associated with a high degree of hydration. We also investigate the effects of the total B-site ionic radii on the hydration thermodynamics. Finally, both electrolyte compositions were integrated into cathode-supported steam electrolysis cells with Ba_{0.5}La_{0.5}CoO_{3- δ} (BLC55) as the anode and Ni as the cathode catalyst. And their electrochemical performance was evaluated.

2. Results and Discussion

2.1. Phase analysis and crystal structure

Figure (1a) illustrates the XRD patterns at room temperature of the Ba(Zr_xCe_{10-x})_{0.08}Y_{0.2}O_{3-\delta} (1 $\le x \le 9$) pellets after sintering and the enlarged 2 θ region between 40 and 45° presented in Figure (1b), confirming single-phase perovskite structures with minor impurities. Refinement of the patterns identified compositions in the nominal 5.5 $\le x \le 9$ range associated with the typical cubic perovskites type structures (space group $Pm\overline{3}m$)^[6,17,24], whereas the range $1 \le x \le 9$ was more or less orthorhombic (space group Pmma).

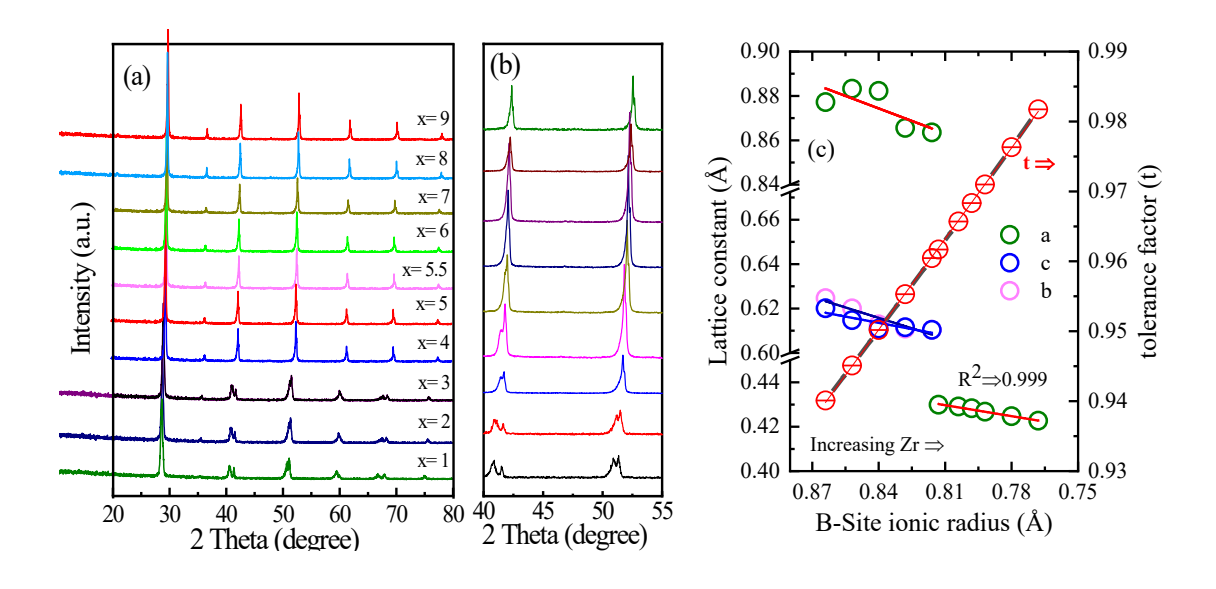


Figure 1. XRD patterns for Ba(Zr_xCe_{10-x})_{0.08}Y_{0.2}O_{3- δ} (1 $\leq x \leq 9$) pellets measured at room temperature with different Zr content. b) Enlarged 2 θ region between 40 and 45°, c) Variation

of the Pseudo-cubic and orthorhombic lattice constants a, b, and c as a function of the B-site ionic radius and the tolerant factor indicating the distortion of the crystal lattice

An angular shift of the XRD pattern towards higher angles is also visible in Figure (1b), reflecting the substitution of Ce⁴⁺ (0.87Å) for the Zr⁴⁺ (0.72Å) in the lattice and shrinkage in the unit cell dimension consistent with previous reports^[17,24,34]. The lattice parameter, unit cell volume, and other physical properties are summarised in Table 1.

Table 1. Summary of the structural and hydration features of Ba(Zr_xCe_{10-x})_{0.08}Y_{0.2}O_{3- δ} with different Zr content: crystal symmetry and lattice parameters, unit cell volume, tolerance factor.

								σ_H /mScm ⁻¹
Composition	Crystal structure	a	b	С	$Å^3$	t	%	600 °C
$BaZr_{0.08}Ce_{0.72}Y_{0.2}O_{3\text{-}\delta}{}^{\rho}$	orthorhmbic	8.7723	6.2467	6.2008	339.98	0.9401	96.6	21.9
$BaZr_{0.16}Ce_{0.64}Y_{0.2}O_{3\text{-}\delta}{}^{\rho}$	orthorhmbic	8.8328	6.2678	6.1475	340.34	0.9451	97.9	20.0
$BaZr_{0.24}Ce_{0.56}Y_{0.2}O_{3\text{-}\delta}\ ^{\rho}$	orthorhmbic	8.8228	6.2637	6.1093	337.62	0.9502	95.8	14.5
$BaZr_{0.32}Ce_{0.48}Y_{0.2}O_{3\text{-}\delta}{}^{\rho}$	orthorhmbic	8.6557	6.1209	6.1158	324.02	0.9657	96.4	12.6
$BaZr_{0.4}Ce_{0.4}Y_{0.2}O_{3\text{-}\delta}{}^{\rho}$	orthorhmbic	8.6352	6.1083	6.1038	321.95	0.9605	96.5	11.1
$BaZr_{0.44}Ce_{0.36}Y_{0.2}O_{3\text{-}\delta}{}^{\chi}$	cubic	4.2986	4.2986	4.2986	79.4310	0.9617	98.3	14.5
$BaZr_{0.48}Ce_{0.32}Y_{0.2}O_{3\text{-}\delta}{}^{\chi}$	cubic	4.2851	4.2851	4.2851	78.6834	0.9657	95.8	13.1
$BaZr_{0.52}Ce_{0.28}Y_{0.2}O_{3\text{-}\delta}{}^{\chi}$	cubic	4.2830	4.2830	4.2830	78.5664	0.9657	95.7	10.9
$BaZr_{0.56}Ce_{0.24}Y_{0.2}O_{3\text{-}\delta}{}^{\chi}$	cubic	4.2810	4.2810	4.2810	78.4007	0.9710	96.4	10.8
$BaZr_{0.64}Ce_{0.16}Y_{0.2}O_{3\text{-}\delta}{}^{\chi}$	cubic	4.2676	4.2676	4.2676	77.7229	0.9763	95.9	9.90
BaZr _{0.72} Ce _{0.08} Y _{0.2} O _{3-δ} ^χ	cubic	4.241	4.241	4.241	76.3163	0.9817	97.5	8.10
ρ; space group Pnma, Z χ; space group Pm3m, Z					•		•	•

relative density obtained on sintered pellets, and the conductivity at 600 °C

To further verify the formation of the solid solution, the calculated pseudo-orthorhombic and cubic lattice constants were plotted against the B-site ionic radius (Figure (1c)) using values given by Shannon^[35]. A somewhat linear dependence is observed, suggesting Ce and Zr are statistically distributed in the lattice and that the solid solution exits within the studied range of

Ba(Zr_xCe_{10-x})_{0.08} $Y_{0.2}O_{3-\delta}$ compositions^[24,36]. For all the compositions, the Goldschmidt tolerance factor calculated using Equation (3) is 0.94 ~0.98, indicating a stable pseudo-orthorhombic and cubic phase, with the most distorted structure associated with the largest B-site ionic radius (Ba $Zr_{0.08}Ce_{0.72}Y_{0.2}O_{3-\delta}$).

$$t = \frac{r_A + r_O}{\sqrt{2(r_B + r_O)}}....$$

2.2. Dependence of electrical conductivity on Zr/Ce ratio in Ba(Zr, Ce, Y)O_{3-δ} system

Plots of the electrical conductivity measured in moist atmospheres using a 4-probe dc method described elsewhere^[6] are illustrated in figure 2 (a, b). As apparent from Figure 2 (b), the total conductivity in wet air for most of the studied compositions is slightly higher than that measured in moist hydrogen (Figure 2 a), especially within the range of 700 °C and 800 °C. This increase in conductivity is possibly due to electron-hole, and oxygen ion conduction, which is consistent with previous reports and is discussed later in this manuscript^[6,29]. Whereas the total conductivity in wet hydrogen mainly consists of proton conduction.

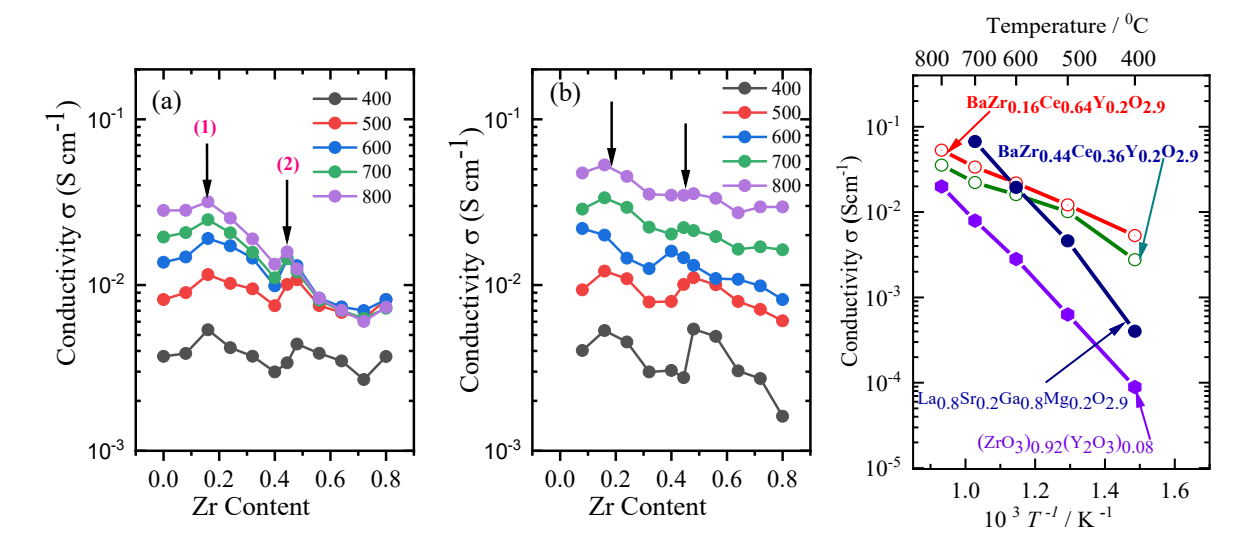


Figure 2. Total electrical conductivity isotherms of Ba(Zr_xCe_{10-x})_{0.08}Y_{0.2}O_{3-δ} in (a) humid 1%H₂ as a function of temperature and (b) humid air as a function of temperature; (c) Comparison of the ionic conductivities of BaZr_{0.44}Ce_{0.36}Y_{0.2}O_{3-δ}, BaZr_{0.16}Ce_{0.64}Y_{0.2}O_{3-δ}, LSGM, and YSZ measured at 400° to 800°C.

Partial substitution of Ce in the system by Zr induced a slight variation in the conductivities within the 700 °C and 800 °C range in wet air compared to wet hydrogen ($P_{\rm H2O} = 1.9 \times 10^3 \, \rm Pa$). It is perhaps not surprising that the Ce-rich compositions have better conductivity than the Zrrich counterparts. Nonetheless, a more relevant effect here is the appearance of two composition ranges where the conductivity is almost constant or increases with Zr content, with maximum conductivity values at the points labeled (1) and (2) in red (Figure 2a). This observation contrasts with other reports suggesting a linear decrease in conductivity with increasing zirconium. Instead, at 500 °C and 400 °C, there is a composition range where the conductivity increases with increasing zirconium content. For example, at 500 °C, the ionic conductivity observed in a water vapor saturated atmosphere is 10.1 and 11.5 mS/cm, respectively, for both points. Moreover, The total conductivities of BaZr_{0.44}Ce_{0.36}Y_{0.2}O_{3-δ} and BaZr_{0.16}Ce_{0.64}Y_{0.2}O_{3-δ} obtained below 600 °C are higher than those of LSGM and YSZ, which are some of the most frequently used benchmarks for oxide ion conducting solid electrolytes (Figure (2c)). Although the Zr/Ce mixing on the perovskite B-site was initially anticipated to reduce the protonic mobility, probably, the corresponding lattice expansion from the BaZr_{0.44}Ce_{0.36}Y_{0.2}O_{3-δ} composition and its cubic symmetry seems beneficial for protonic mobility. Finally, it is worth pointing out that current state-of-the-art Ba($Zr_{0.1}Ce_{0.7}Y_{0.2}$)O_{3-\delta}(9×10⁻³ S/cm at 500 °C)^[37] and BaZr_{0.1}Ce_{0.7}Y_{0.1}Yb_{0.1}O_{3- δ} compositions, though with similar conductivity [38] as well, reacts with CO₂ and H₂O even under mild conditions^[39]. Thus, the present BaZr_{0.44}Ce_{0.36}Y_{0.2}O_{3-δ} exhibits a good conductivity and stability trade-off, as discussed in the later section.

To further understand the conductivity trend as a function of Zr content, proton concentration in the samples was estimated using thermogravimetric analysis by correlating the weight increase from water uptake to the concentration of protons as reported in the experimental section. Figure 3(a) shows the composition dependence of the proton concentration obtained from the weight change. The amount of incorporated water is the ratio of the quantity of water over that of $Ba(Zr_xCe_{10-x})_{0.08}Y_{0.2}O_{3-\delta}$ oxide expressed in mol mol⁻¹. As

observed, the proton concentration increases with temperature, and the trend is somewhat similar to that of the conductivity. Figure 3(b, c) also presents the proton concentrations for BaZr_{0.44}Ce_{0.36}Y_{0.2}O_{3-δ} and BaZr_{0.16}Ce_{0.64}Y_{0.2}O_{3-δ} as a function of reciprocal temperature along with modeled curves generated by fitting the data with similar procedures reported in reference^[6,30,40]. From the Figure, the incorporation of water increases with decreasing temperature (1200–200 °C) for both compositions, reflecting the hydration reaction's exothermic nature.

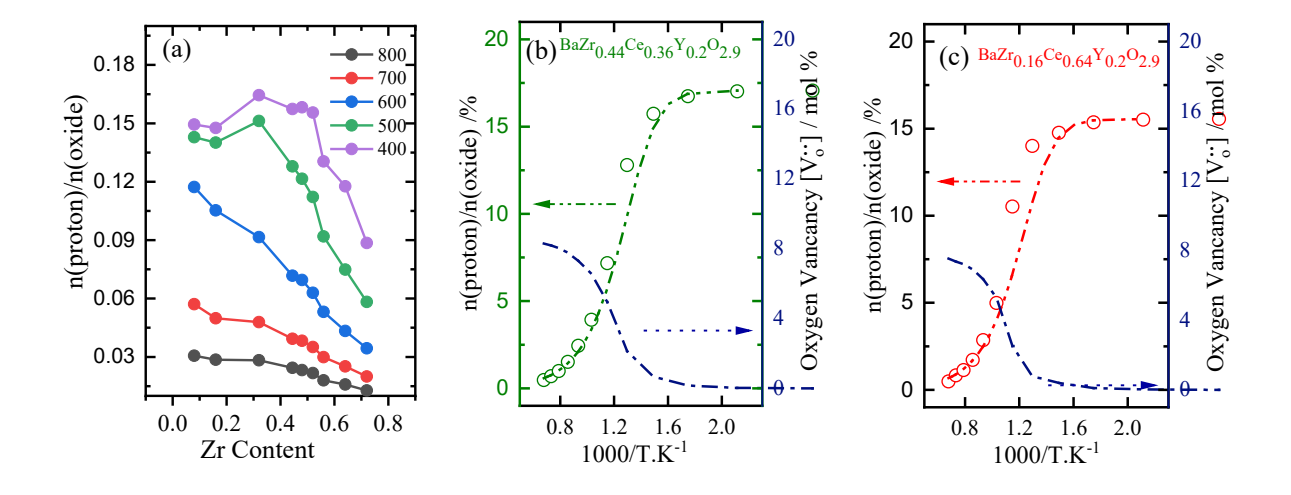


Figure 3. Equilibrium proton concentrations of $Ba(Zr_xCe_{10-x})_{0.8}Y_{0.2}O_{3-\delta}$. (a) Compositional dependence of the proton concentration as a function of Zr content. Temperature dependence of the proton concentration in (b) $BaZr_{0.44}Ce_{0.36}Y_{0.2}O_{3-\delta}$ and (c) $BaZr_{0.16}Ce_{0.64}Y_{0.2}O_{3-\delta}$. The red and green dotted lines are the curve-fitted proton concentrations.

It is worth pointing out that the total proton uptake of 0.17 and 0.15-mole fractions for BaZr_{0.44}Ce_{0.36}Y_{0.2}O_{3-δ} (85.3% vs. nominal doping level) and BaZr_{0.16}Ce_{0.64}Y_{0.2}O_{3-δ} (77.5%) is lower than expected from the nominal doping level of 0.2, even though the conductivity of the latter is higher. This phenomenon is not uncommon with other prominent proton-conductors ^[6,7,12]. This behavior has been suggested to stem from BaO loss and subsequent incorporation of the dopant cation onto the A-site, where it acts as a donor ^[41,42]. It is also important to point

out that Ba over stoichiometry to compensate for Ba loss was not employed in the present study. Thus, high conductivity in acceptor doped BaZrO₃-BaCeO₃ solid solutions depends not solely on the protonic concentration but also on the antagonistic effects of local ordering, symmetry reduction, and the respective charge carriers in the said composition^[9,23,24]. Protonic defects are not the sole charge carriers in these perovskite-type oxides^[13,18,43]. The total conductivity in this class of material also constitutes contributions from other charge carriers: oxygen ion, V_o^- ; electron-hole, σ_h^- ; electron, $\sigma_{e'}$; and proton conduction, σ_H . The role of each carrier varies with gas composition and temperature. The total conductivity (σ_t) can thus be obtained using Equation (4):

$$\sigma_t = \sigma_{V_o^{\cdot \cdot}} + \sigma_{h^{\cdot}} + \sigma_{e'} + \sigma_{H^{\cdot}}$$

$$= \frac{F}{V_m} (2[V_o^{\cdot \cdot}] \mu_{V_o^{\cdot \cdot}} + [h^{\cdot}] \mu_{h^{\cdot}} + [e^{\prime}] \mu_{e^{\prime}} + [H^{\cdot}] \mu_{H^{\cdot}})...$$
(4)

where F is the Faraday constant; V_m is the molar volume, $[V_0^{"}]$, $[h^{"}]$, $[e^{'}]$ and $[H^{"}]$ the molar concentration of oxygen vacancies, holes, electrons, and protons, respectively, whereas $\mu_{V_0^{"}}$, $\mu_{h^{"}}$, $\mu_{e^{'}}$, and $\mu_{H^{"}}$ the corresponding mobilities. The electronic contribution to the total conductivity of both BaZr_{0.44}Ce_{0.36}Y_{0.2}O_{3- δ} and BaZr_{0.16}Ce_{0.64}Y_{0.2}O_{3- δ} can thus be understood by measuring their dependence on oxygen partial pressure. At equilibrium conditions, both compositions can exchange oxygen with the surrounding atmosphere, according to Equation 2.

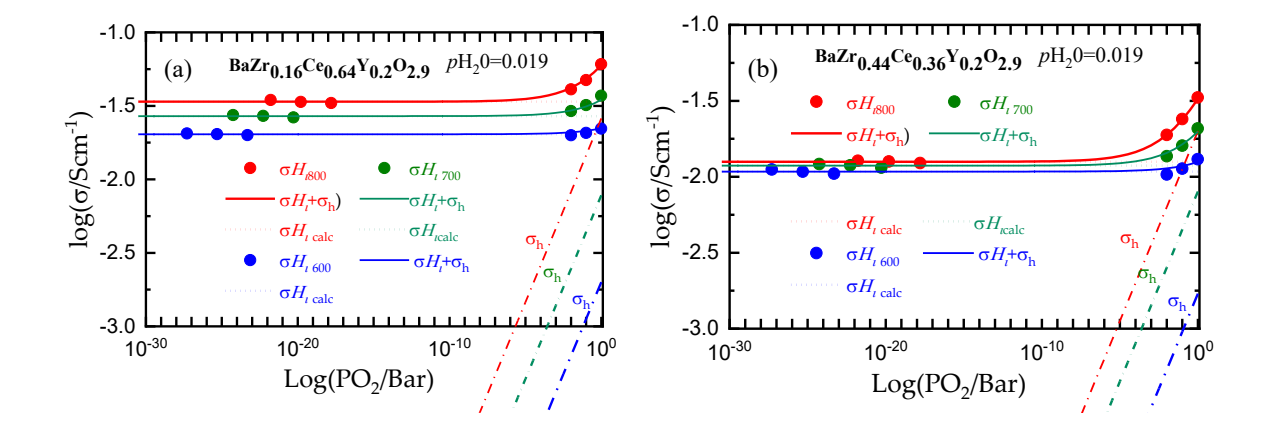


Figure 4. The dependences of total electrical conductivity on the oxygen partial pressure in the temperature range between 600 °C and 800 °C. (a) BaZr_{0.16}Ce_{0.64}Y_{0.2}O_{2.9} (b) BaZr_{0.44}Ce_{0.36}Y_{0.2}O_{2.9}

The dependence of the measured and fitted conductivity for both electrolytes on oxygen partial pressure (P_{O_2}) is depicted in Figure 4 for the 600, 700, and 800 °C temperature range. As observed, the conductivity is essentially independent of P_{O_2} , indicating that, under such conditions, proton conduction dominates over a wide range of P_{O_2} , but proportional to 1/4 power of P_{O_2} , at high oxygen, partial pressures were the σ_{h^-} starts to prevail. This trend is consistent with other analogous acceptor-doped perovskite-type oxides^[13,17,43].

2.3. Thermodynamics of hydration in Ba(Zr_xCe_{10-x})_{0.08}Y_{0.2}O_{3-δ} compositions

Hydration of acceptor doped perovskites is generally accompanied by a distortion in the lattice, commonly referred to as chemical volumetric expansion^[12,13,44]. Therefore, a proper understanding of these concepts is critical in developing new electrolytes. For the sake of comparison, two other acceptor dopants (Sc, Gd) were prepared with a similar Ce/Zr ratio of 5/4 at the perovskite B-site to understand the latter behavior. Figure 5 (a, b) shows the temperature dependence of the lattice volume measured by high-temperature XRD with heating in 1% hydrogen and cooling in a vacuum. While the lattice volume trends in the order of Gd> Y> Sc, corresponding to the size of the dopant, the magnitude of chemical expansion (ΔV) is Y> Gd> Sc, similar to the conductivity trend in Figure S1, Supporting Information. In other words, the higher the conductivity, the more significant the chemical expansion. The observed trend is reasonable considering that chemical expansion emanates from hydration, leading to protonic conductivity. Nonetheless, a more desirable electrolyte should have high conductivity and minimal chemical expansion. Figure 5(b) shows the conductivity at 600 °C plotted against the chemical expansion from the respective dopants. As observed, the stiffer the slope, the

higher the conductivity at the same chemical expansion (i.e., lower chemical expansion at the same conductivity). Thus Y is the most desirable dopant among the three dopants.

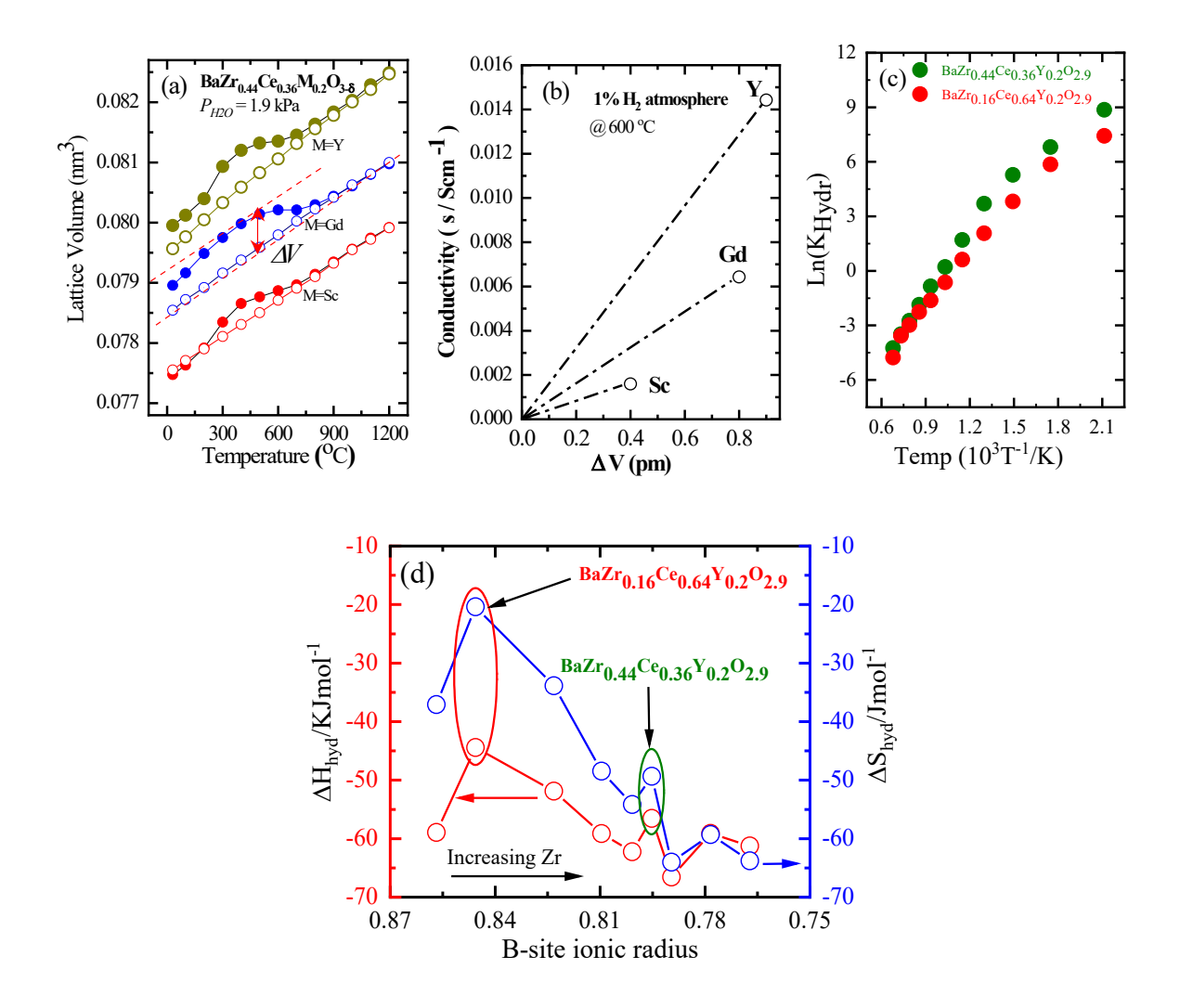


Figure 5. (a) Temperature dependence of lattice volume of BaZr_{0.44}Ce_{0.36}M_{0.2}O_{2.9} (M=Sc, Gd, Y) determined by HT-XRD measurements, the marked data points represent heating in 1% H₂-balance Ar atmosphere. In contrast, the open data points represent cooling in a vacuum. (b) Relationship between chemical expansion and electrical conductivity at 600°C. (c) The equilibrium constant for the hydration reaction, calculated for BaZr_{0.16}Ce_{0.64}Y_{0.2}O_{2.9} and BaZr_{0.44}Ce_{0.36}Y_{0.2}O_{2.9}. (d) Hydration enthalpies and entropies as a function of B-site ionic radius.

The thermodynamic parameters describing the defect chemistry of the as-synthesized $Ba(Zr_xCe_{10-x})_{0.08}Y_{0.2}O_{3-\delta}$ compositions can be extracted through the equilibrium constants

associated with the hydration reaction (Equation 1 above). The corresponding equilibrium constant for the reaction can be written as follows:

$$K_{hyd} = \frac{[OH_O^*]^2}{P_{H_2O}[V_O^*][O_O^*]} = exp \frac{\Delta S_{hyd}}{R} exp \frac{-\Delta H_{hyd}}{RT}.$$

 K_{hyd} is the equilibrium constant for hydration reaction, ΔH_{hyd} and ΔS_{hyd} are the hydration enthalpy and entropy, respectively. The hydration enthalpy and entropy in the current system are considered based on previously reported assumptions, involving two types of oxide ion vacancies, one of which is hydrated and the other immobile (inert oxide ion vacancy)^[6,7]. The nominal acceptor concentration can be charge compensated using the following expression; where $[Y'_{\textit{Ce or Zr}}]$ is the concentration of Y at either the Ce or Zr sites, $[Hi\cdot]$ represents the proton concentration, while $\left[V_{o\,(1)}^{\cdot\cdot}\right]$ and $\left[V_{o\,(2)}^{\cdot\cdot}\right]$ denote hydrated oxide ion vacancy involved in hydration and inert oxide ion vacancy, respectively, and the hole concentration is considered negligible. By setting the inert oxide ion vacancy $(2[V_{o(2)}] = [Y'_{Ce\ or\ Zr}] - [OH_o]_{limit})$, as the fit parameter with $[OH_o]_{limit}$ = the hydration limit described above. Thus, the equilibrium constant can be calculated using the proton concentration data measured from TGA, Equations 5 and 6 as a function of the reciprocal temperature, as shown in the van't Hoff plot (Figure 5c) for BaZr_{0.16}Ce_{0.64}Y_{0.2}O_{2.9} and BaZr_{0.44}Ce_{0.36}Y_{0.2}O_{2.9}. The presence of two distinct regions with different characteristic behaviors is observed. A low-temperature linear part, similar to that observed by Yamazaki et al. [44] and Lim et al. [45], whereas, at high temperatures, the behavior deviates from linearity with a change in slope, at approximately 500 °C, consistent with previous reports. The latter behavior has been attributed to possible influences from electronic defects and changes in oxygen content at high temperatures, particularly for Ba-containing perovskites. [42,44-46]. As a consequence, extracted ΔH_{hyd} and ΔS_{hyd} values from a wide temperature range may present some inconsistency. Thus both parameters were evaluated from analyses restricted to low temperatures at which K_{hyd} behaves somewhat more linearly on the

Arrhenius plot. The resulting hydration enthalpies and entropies extracted were in the range -44.4 to -66.6 kJ mol⁻¹ and -20.4 to -64.04 J K⁻¹ mol⁻¹, respectively. Figure 5(d) presents the extracted ΔH_{hyd} and ΔS_{hyd} values plotted as a function of Zr content. As observe the lower ionic radii compositions (higer Zr content), display the least favourable hydration enthalpies. Hydration enthalpy should, in principle, decrease (more exothermic) with increasing ionic radius or decreasing electronegativity of the acceptor as this effectively lowers the tolerance factor ^[42,46,47]. These properties ultimately relate to the bonding strengths of oxide ions and protons, as previously hypothesized by Bjørheim et al. ^[48], and are consistent with the present observation. Even though no clear-cut dependence on Zr content or the B-site ionic radius is apparent, the trend for both values is somewhat similar to previously reported ^[48,49] trends observed for the proton concentration discussed above. A summary of the extracted thermodynamic parameters is presented in Table 2

Table 2. Thermodynamics properties (ΔH_{hyd} and ΔS_{hyd} obtained through linearization), estimated proton saturation limits, and the concentration of inert oxygen vacancy of the asprepared samples

Composition	$\Delta H(kJmol^{-1})$	$\Delta S(J mol^{-1}k^{-1})$	$[H_i]_{limit}$	$[V_{o(2)}^{"}].$	V_m (cm 3)	Hydration (%)
BaZr _{0.08} Ce _{0.72} Y _{0.2} O _{3-δ}	-58.9363	-37.1046	0.1567	0.0216	51.19	78.37
BaZr _{0.16} Ce _{0.64} Y _{0.2} O _{3-δ}	-44.4175	-20.3942	0.1557	0.0222	51.25	77.75
$BaZr_{0.32}Ce_{0.48}Y_{0.2}O_{3-\delta}$	-51.8694	-33.8712	0.1750	0.0125	48.79	87.52
BaZr _{0.44} Ce _{0.36} Y _{0.2} O _{3-δ}	-59.1408	-48.4581	0.1706	0.0147	47.84	85.52
BaZr _{0.48} Ce _{0.32} Y _{0.2} O _{3-δ}	-62.2494	-54.169	0.1724	0.0138	47.39	86.24
BaZr _{0.52} Ce _{0.28} Y _{0.2} O _{3-δ}	-56.5244	-49.3494	0.1768	0.0116	47.32	88.40
BaZr _{0.56} Ce _{0.24} Y _{0.2} O _{3-δ}	-66.5469	-64.0278	0.1485	0.0257	47.22	74.27
Ba $Zr_{0.64}Ce_{0.16}Y_{0.2}O_{3-\delta}$	-59.1009	-59.3046	0.1497	0.0252	46.81	74.82
BaZr _{0.72} Ce _{0.08} Y _{0.2} O _{3-δ}	-61.2584	-63.7784	0.1129	0.0436	45.97	56.48

2.4. Chemical stability

Despite the high conductivity of current state-of-the-art acceptor doped $BaZrO_3$ - $BaCeO_3$ perovskite-type proton-conductors ($BaZr_{0.1}Ce_{0.7}Y_{0.2}O_{3-\delta}$, or $BaZr_{0.1}Ce_{0.7}Y_{0.1}Yb_{0.1}O_{3-\delta}$), their stability in atmospheres containing water vapor, CO_2 , or hydrocarbons remains a significant concern^[21,27,29]. Their reactivity with CO_2 generally results in the decomposition of the

perovskite structure into barium carbonate and cerium oxide and a deterioration of their mechanical properties^[50,51]. The reaction can be reasonably described according to the Kröger–Vink notation using Equation 7.

Where V_{Ba} and V_0 denotes Ba- and O-vacancies, respectively. Therefore, reactivity becomes even more critical for systems with high cerium content in the composition. However, intermediate contents of both Zr and Ce in Y doped BaZrO₃-BaCeO₃ solid solutions are expected to improve the thermodynamic stability while simultaneously achieving acceptable conductivity. Therefore, to assess the chemical stability of the synthesized specimens, sintered powders of some selected nominal intermediate compositions (BaZr_{0.24}Ce_{0.56}Y_{0.2}O_{2.9}, BaZr_{0.44}Ce_{0.36}Y_{0.2}O_{2.9}, and BaZr_{0.56}Ce_{0.24}Y_{0.2}O_{2.9}) were exposed to 100 % CO₂, and their reactivity was evaluated by monitoring any gain in weight using thermogravimetric analyses. Figure 6 (a-c) presents the TGA profile of the compositions upon exposure to 100 % CO₂.

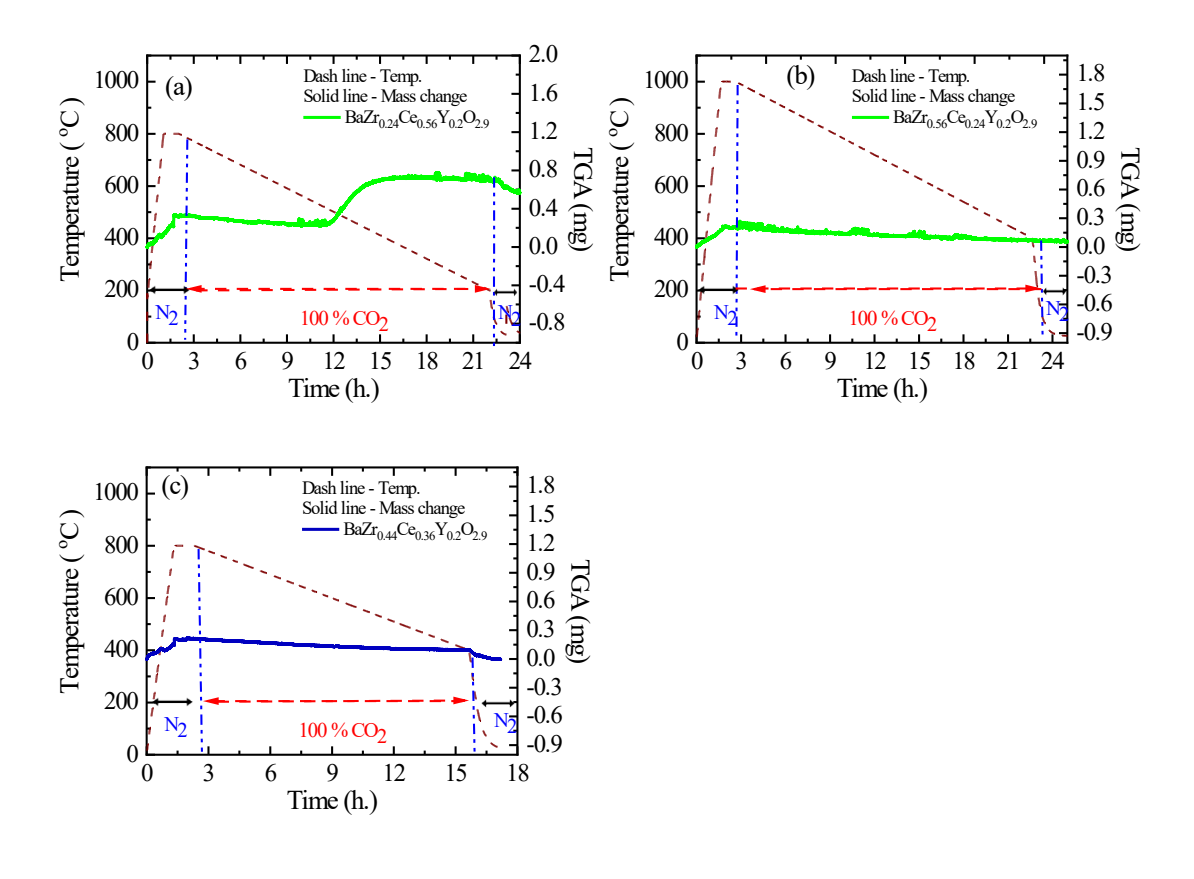


Figure 6. TGA profiles for (a) $BaZr_{0.24}Ce_{0.56}Y_{0.2}O_{2.9}$; (b) $BaZr_{0.44}Ce_{0.36}Y_{0.2}O_{2.9}$; and (c) $BaZr_{0.56}Ce_{0.24}Y_{0.2}O_{2.9}$ upon exposure to 100 vol % CO_2

A partial reaction between composition BaZr_{0.24}Ce_{0.56}Y_{0.2}O_{2.9} and CO₂ is apparent as weight is gained commencing at 500 °C (figure 6 a), associated with the material's reactivity with CO₂. In contrast, 24 % and 36 % lower cerium concentration in the BaZr_{0.56}Ce_{0.24}Y_{0.2}O_{2.9} and BaZr_{0.44}Ce_{0.36}Y_{0.2}O_{2.9} compositions show no mass change or remain stable in 100 % CO₂ as the temperature decreases to room temperature. The observation is consistent with analogous acceptor doped Zr-rich perovskites type oxides^[17,21,51]. Therefore, based on the above finding, BaZr_{0.44}Ce_{0.36}Y_{0.2}O_{3-δ} seems the better choice electrolyte and should be promising for PCEC/PCFC.

2.5. Steam electrolysis

BaZr_{0.16}Ce_{0.64}Y_{0.2}O_{2.9} and BaZr_{0.44}Ce_{0.36}Y_{0.2}O_{2.9} electrolyte compositions were integrated into cathode-supported steam electrolysis cells with BLC55 as the anode and Ni as the cathode catalyst. Both cells were fabricated using a well-established low-cost, sequential tape casting processing route [52–54]. The cathode support NiO-SrZr_{0.5}Ce_{0.4}Y_{0.1}O_{2.95} layer adheres well to the electrolyte layer forming an excellent percolating network, which should, in principle, lead to more triple-phase boundaries and, thus, enhance the cathodic reaction. Figure 7 (e, f) shows typical I–V characteristics measured under the supply of humidified 20 vol. % H₂O diluted with 1 vol. % O₂-99 % Ar to the anode and 1 vol.% vol H₂-Ar 99 vol. % at the cathode, for both BaZr_{0.16}Ce_{0.64}Y_{0.2}O_{2.9} and BaZr_{0.44}Ce_{0.36}Y_{0.2}O_{2.9} electrolyte-based cells. At an applied voltage of 1.3 V, the BaZr_{0.44}Ce_{0.36}Y_{0.2}O_{2.9} cell reaches electrolysis current densities of 500 and 250 mA /cm² at 600 and 550 °C. In contrast, the BaZr_{0.16}Ce_{0.64}Y_{0.2}O_{2.9} based cell reaches 600 and

250 mA /cm² under similar conditions, respectively, which are among the best performances reported at these temperatures for these perovskite-type oxides^[1,3,16,55–60].

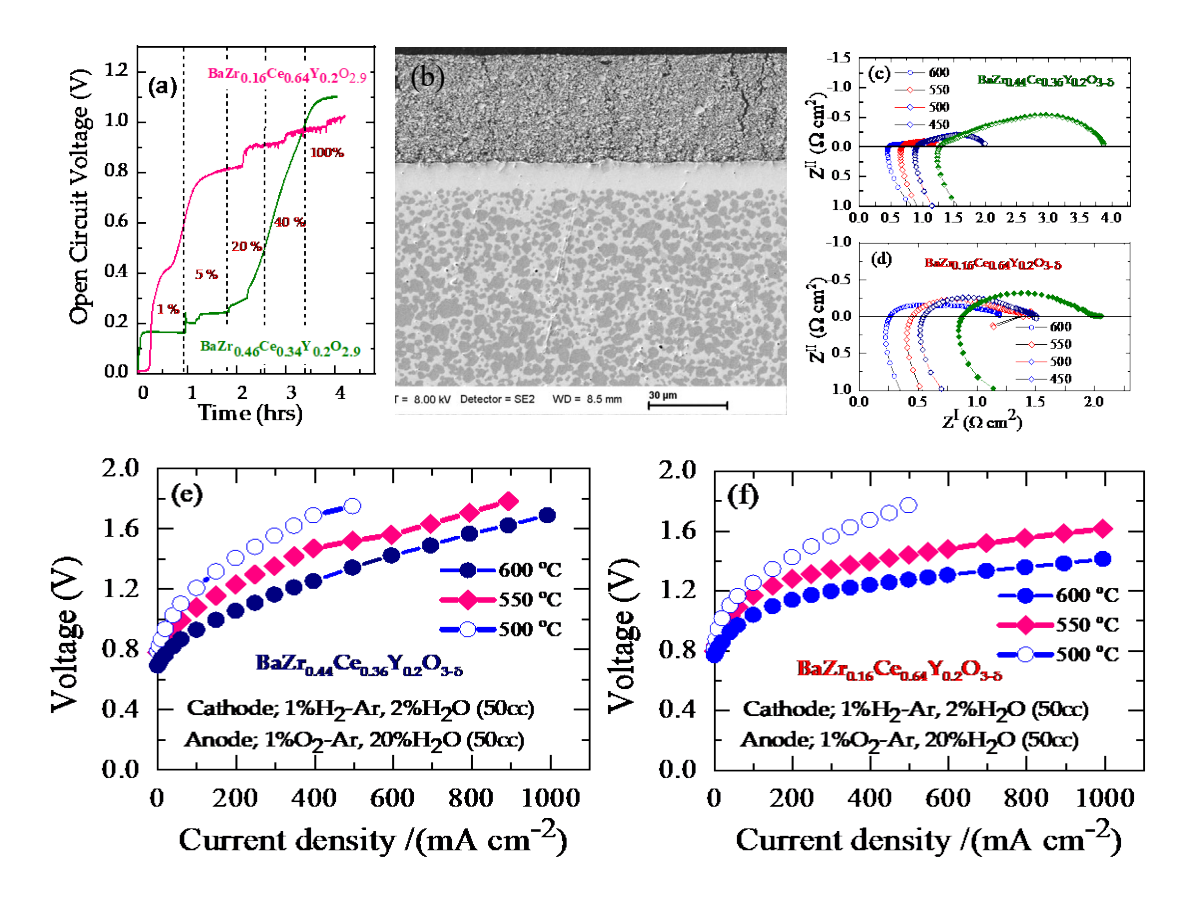


Figure 7 (a) Open circuit voltage profiles for BaZr_{0.16}Ce_{0.64}Y_{0.2}O_{2.9} and BaZr_{0.44}Ce_{0.36}Y_{0.2}O_{2.9} electrolyte-based cells obtained during the cathode reduction at 600 °C. (b) Typical cross-sectional SEM image of the fabricated cell (c) EIS spectra of the cathode-supported BaZr_{0.44}Ce_{0.36}Y_{0.2}O_{2.9} cell after reduction. (d) EIS spectra of the cathode-supported BaZr_{0.16}Ce_{0.64}Y_{0.2}O_{2.9} cell. (e) Typical I–V characteristics for a steam electrolysis cell based on BaZr_{0.44}Ce_{0.36}Y_{0.2}O_{2.9} electrolyte. (f) Typical I–V characteristics for a steam electrolysis cell based on BaZr_{0.16}Ce_{0.64}Y_{0.2}O_{2.9} electrolyte.

It is also worth mentioning that the present cell performance is also affected by the low catalytic activity of the anode (BLC55), a typical oxygen-conducting material^[61]. The slightly enhanced performance at 600 °C for the latter electrolyte can be accredited to its lower ohmic resistance

due to higher electronic conductivity. Figure 7 (c, d) presents the impedance spectra of the cells obtained under open-circuit conditions. As indicated, both electrolytes' ohmic resistances under OCV conditions were $0.26-0.87~\Omega~cm^2$ and $0.46-1.27~\Omega~cm^2$ at $600-450~^{\circ}$ C, respectively, however higher than that reported for other high-performance PCECs. Whereas the electrode resistances mainly dominate the total cell resistance. Hence, further reduction of the electrolyte thickness and a new highly active air electrode explicitly tailored for protonic electrolytes is expected to boost the cell performance by lowering its ASRs. Table 3 summarizes the performance of some recently investigated PCEC with Y doped BaZrO₃-BaCeO₃ perovskite-type electrolytes.

Table 3 Comparison of steam electrolysis performance demonstrated with similar electrolyte type cells

	Test condition	Cell p			
Cell configuration	Anode gas pressure (electrolyte thickness)	Cathode gas pressure	J/Acm ⁻² @ 1.3V .temp/°C	η_{Fex} %	Year Ref
NBSCF-BCZYYb BCZYYb Ni-BCZYYb	10% H ₂ O, air (20μm)	90% H ₂ (10% H ₂ O	0.75 (600)	N/A	201855
BSCF-BCZY62 BCZY62 Ni-BCZY	2.8% $H_2O,$ air (15 $\mu m)$	50% H ₂ (2.8% H ₂ O)	1.05 (600)	N/A	201316
LSC-BZCYbCo BZCYbCo Ni-BZCY	30% H ₂ O, 19% O2, 45μm	10 % H ₂ /He	0.03 (600)	85	2011 ⁵⁹
SEFC-BCZY35 BCZY35 Ni-BCZY	10% H ₂ O/Air(15μm)	97% H ₂ (3% H ₂ O)	0.42(600)	33	2018 ⁶⁰
BCZFY BZCYYb7211 Ni- BZCYYb	20% H ₂ O, 97% air (5μm)	97% H ₂ (3% H ₂ O)	1.00 (600)	97	2019 ³
PBSCF BZCYYb411 Ni- BZCYYb	3% H ₂ O, 97% air (15μm)	97% H ₂ (3% H ₂ O)	1.31(600)	75	2019 ¹
LNF/LN BZCD(30µm) Ni-BZCD	3% H ₂ O, 97% air (30μ m)	97% H ₂ (3% H ₂ O)	0.3 (600)	N/A	2016 ⁵⁸
SSC-BZCY53 BZCY53 Ni-BZCY53	50% H ₂ O, 50% air (20μm)	97% H ₂ (3% H ₂ O)	0.33 (600)		2010 ⁵⁷
$SSC\text{-}BZCY BZCY442(15\mu m) Pt$	20% H ₂ O, air (1.5mm)	1% H ₂ (3% H ₂ O)	0.04 (600)	70	2018 ⁵⁶
BLC BZCY(28)82 Ni-SZCY541	20% H ₂ O/1%O ₂ (12μm)	1% H ₂ - 2% H ₂ O	0.6 (600)	81.5	This Wk
BLC BZCY(54)8/92 Ni-SZCY541	20% H ₂ O/1%O ₂ (12μm)	1% H ₂ - 2% H ₂ O	0.5 (600)	76.8	This Wk

 $BZCY(28)_{8}2 = BaZr_{0.16}Ce_{0.64}Y_{0.2}O_{3-\delta},\ BZCY(28)_{8/9}2 = BaZr_{0.44}Ce_{0.36}Y_{0.2}O_{3-\delta},\ BZCY(28)_{8/9}2 = BaZr_{0.44}Ce_{0.36}Y_{0.2}O_{0.44}Ce_{0.36}Y_{0.2}O_{0.44}Ce_{0.36}Y_{0.2}O_{0.44}Ce_{0.36}Y_{0.2}O_{0.44}Ce_{0.36}Y_{0.2}O_{0.44}Ce_{0.36}Y_{0.2}O_{0.44}Ce_$

 $\eta_{\textit{Fex}} = \text{Current efficiency}, \; BZY82 = BaZr_{0.8}Y_{0.2}O_{3-\delta}, \\ SFM = Sr_2Fe_{1.5}Mo_{0.5}O_{6-\delta}, \\ BZY = BaZr_{0.9}Y_{0.1}O_{3-\delta}, \\ Wk = Work + Work$

 $BCZYbCo = BaCe_{0.48}Zr_{0.40}Yb_{0.10}Co_{0.02}O_{3-\delta}, BCZD = BaCe_{0.5}Zr_{0.3}Dy_{0.2}O_{3-\delta}, BCZY81 = BaCe_{0.8}Zr_{0.1}Y_{0.1}O_{3-\delta}, SDC = BaCe_{0.8}Zr_{0.1}Y_{0.1}O_{3-\delta}$

 $Ce_{0.8}Sm_{0.2}O_{2-\delta},\ BCZY44=BaCe_{0.4}Zr_{0.4}Y_{0.2}O_{3-\delta},\ BCZYZn=BaCe_{0.5}Zr_{0.3}Y_{0.16}Zn_{0.04}O_{3-\delta},\ BCZY53=BaCe_{0.5}Zr_{0.3}Y_{0.2}O_{3-\delta},\ BCZY53=BaCe_{0.5}Zr_{0.3}Y_{0.2}O_{3-\delta}$

 $BSCF = Ba_{0.5}Sr_{0.5}Co_{0.8}Fe_{0.2}O_{3-\delta}, \ NBSCF = NdBa_{0.5}Sr_{0.5}Co_{1.5}Fe_{0.5}O_{5+\delta}, \ LNF/LN = LaNi_{0.6}Fe_{0.4}O_{3-\delta} \ / \ La_2NiO_{4+\delta} = LaNi_{0.6}Fe_{0.2}O_{3-\delta} \ / \ LaNi_{0.6}Fe$

Figure. 8 (a, b) presents the hydrogen production rate in the steam electrolysis operated at 550 and 600 °C as a function of current density. As the applied current increases, the measured molar hydrogen generation rate deviates from the theoretical rate (estimated from Faraday's

law). For example, the current efficiency was 81.5 and 83.1 % at 600 and 250 m Acm^{-2} for the $BaZr_{0.16}Ce_{0.64}Y_{0.2}O_{2.9}$ cell.

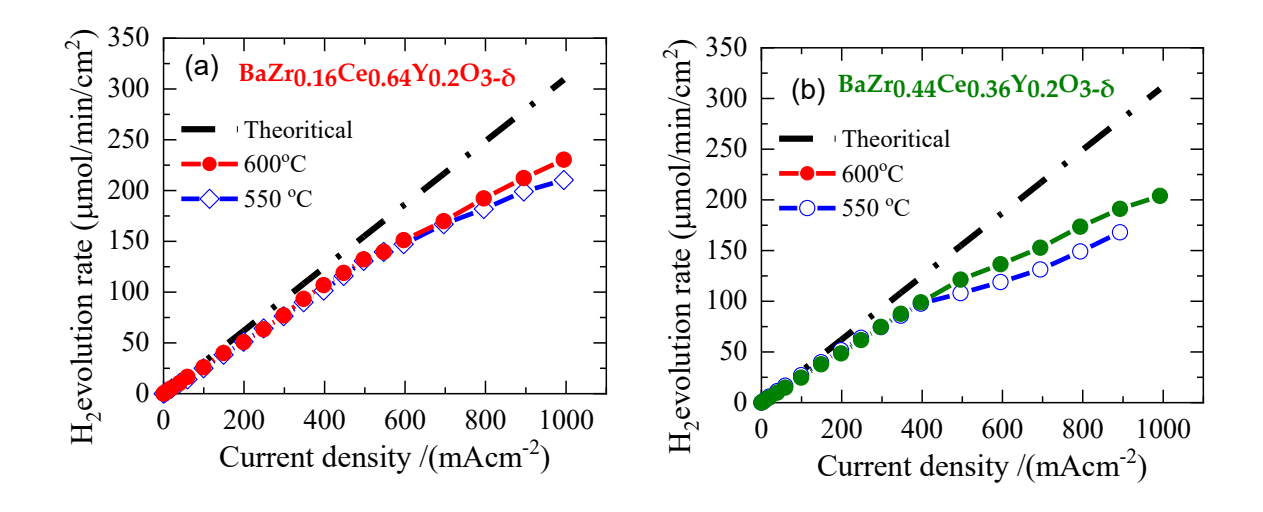


Figure 8. Hydrogen evolution rate measured at 600 and 550 °C under the supply of humidified 20 % H₂O diluted with 1 % O₂ -99 % Ar to the anode and 1% H₂-Ar 99 % at the cathode

Whereas 78.5 and 82.7 % at 500 and 250 m Acm⁻² was obtained with the BaZr_{0.44}Ce_{0.36}Y_{0.2}O_{2.9} based cell respectively at 600°C. These values and other cell properties are summarised in Table 1(SI). A plausible reason for the substantial deviations of the current efficiency, particularly at 500°C, originates from intrinsic electron-hole conduction through the electrolytes and the limited catalytic activity of the anode material BLC^[61], as mentioned above. Currently, we are developing a new highly active air electrode material explicitly tailored for protonic electrolytes to remedy this situation. In perspective, based on our findings, the calculated amount of electricity to produce 1 Nm³ of H₂ is ~3.8 kWh ((1000 L Nm⁻³)/(22.4 L mol⁻¹) × 2*F*/(3600 s h⁻¹) × (1.3V)/0.82)^[52], which is at least 25% reduced from the conventional low-temperature water electrolysis. Additional performance improvement is possible by further decreasing the electrolyte thickness and using anode materials tailored to the present electrolytes.

3. Conclusion

In summary, a systematic approach to further optimize ionic conductivity in $Ba(Zr_xCe_{10-x})_{0.08}Y_{0.2}O_{3-\delta}$, $(1 \le x \le 9)$ oxides for moderate temperature electrolysis was investigated. We found that fixing a cerium/zirconium ratio of 5/4 at the B-site of the perovskite with incremental Zr exhibits two points of conductivity maximum, an observation that contrasts many reports suggesting a linear decrease in conductivity with increasing zirconium in such systems. Furthermore, the resulting $BaZr_{0.44}Ce_{0.36}Y_{0.2}O_{2.9}$ composition showed much-improved stability against CO_2 , with protonic conductivity 10^{-2} S/cm or higher at 500°C. Whereas $BaZr_{0.16}Ce_{0.64}Y_{0.2}O_{3-\delta}$ exhibits the highest electrical conductivity among the studied pellets. Moreover, electrolysis voltage as low as 1.3 V is attainable at current densities of 600 and 250 mA /cm² at 600 and 550 °C, achieving ~81.5 and 83.1 % current efficiencies with the later electrolyte. Based on the above results, the calculated amount of electricity to produce 1 Nm³ of H_2 is ~3.8 kWh¹, which is at least 25 % reduced from the conventional low-temperature water electrolysis.

4. Experimental Section

4.1 Powder Synthesis and Pellet Fabrication;

Powders of Ba(Zr_xCe_{10-x})_{0.08} $Y_{0.2}O_{3-\delta}$, ($1 \le x \le 9$) perovskites type oxides were synthesized using a previously modified chemical solution approach described elsewhere [6,62]. The required amounts (based on desired composition stoichiometry) of Ba(NO₃)₂ (Wako, 99.9%), $ZrO(NO_3)_2$ (Aldrich, 99%), $Ce(NO_3)_3 \cdot 6H_2O$ (Kanto Chemical Co., INC 99.99%), and $Y(NO_3)_3 \cdot 6H_2O$ (Mitsuwa's Pure Chemicals, 99.9 %), EDTA (Dojindo, 99%) and citric acid (Wako, 99%) were dissolved in deionized water. The total metal ions to EDTA and citric acid's molar ratio was 1:1.5:1.5. Ammonium hydroxide solution (Chameleon Regent, 28.0% NH₃ in H₂O) was subsequently added to promote EDTA dissolution and adjust the mixture's pH to \sim 9. After continuous stirring at 160 °C, a dark viscous gel was formed. The gel was pre-heated

at 240 °C in a vacuum oven to obtain a solid black precursor. The as-prepared powders were calcined at 1000 °C for 10 hours and subsequently rolled milled using zirconia balls with ethanol as a solvent for four days to produce uniform, submicrometer particles. The resulting powders were pelletized with a Newton press and further compressed by cold isostatic pressing at 250 MPa. The pellets were then sintered at 1600 °C for 10 hours in a powder bed of the same composition to limit barium evaporation. The nanostructured morphology of the powders facilitated the densification of the pellets. The obtained pellets were subsequently polished using abrasive paper (#250 to #2000) to adjust their dimensions to \sim 13 mm diameter \times 0.5 mm thickness (disk) and 3mm \times 3 mm \times 10 mm (bar) for conductivity measurements.

4.2 Materials characterization

X-ray diffraction (XRD) patterns were acquired at room temperature using a Rigaku Ultima IV X-ray diffractometer with Cu-Kα radiations (λ =1.540598 Å). Diffraction patterns were obtained in the 2θ range between 10 ° and 80 ° with a step size of 0.02° s ⁻¹. The working voltage and current were set at 40 kV and 40 mA during all the measurements. The unit cell parameters were calculated from the Rietveld refined XRD patterns. Bulk densities of the specimens were obtained from their mass and dimensions. Thermogravimetric analysis was performed to quantitatively evaluate the chemical stability of the sintered powders under flowing 100 vol % CO₂. Selected compositions were heated from room temperature to 1050 °C in N₂ and subsequently switched to CO₂ upon cooling. The weight gain due to the specimen's reaction with CO₂ was then evaluated. Powder morphology and fractured surfaces of the sintered samples were observed by a field emission SEM (Hitachi High-Technologies SU8000 equipped with energy-dispersive X-ray spectroscopy (Oxford INCA energy 300 EDS)

4.3 Electrical conductivity measurement

Electrical conductivity was evaluated using electrochemical impedance spectroscopy on bar-

shaped pellets in a 4 a.c., measurement configurations. Platinum paste (Tanaka Kikinzoku Kogyo TR-7907) and platinum lead wires were applied on four points on the bar samples and subsequently fired at 950 °C for 1 hour. Impedance responses were collected with an AC amplitude of 100 mV in the frequency range between 0.1 Hz to 1 MHz using an impedance analyzer (Princeton Applied Research Versa STAT 3), in humidified 1 % H₂ diluted with Ar and wet air ($p(H_2O) = 1.9 \text{ kPa}$) respectively. Before the measurements, samples were held at the measurement temperature for a minimum of 2 -12 hours. Measurements were repeated at least three times to confirm reproducibility.

4.4 Proton concentrations measurement

The proton concentration of the samples was evaluated by thermo-gravimetric analysis (TGA Netzsch STA449F3 Jupiter). Sintered powder samples were first heated in a dry N_2 atmosphere up to 1200 °C and kept for 1 hour to complete sample dehydration. Subsequently, the gas atmosphere was switched to water-saturated Nitrogen Argon (1.9 % H₂O-10 % N₂-Ar, using 10 mL/min dry "protective" gas through balance + 50 mL/min gas saturated with water in a bubbler at 17 °C) and cooled in increments of 100 °C with 2 hours stabilization time per step. Weight changes of the samples were then measured in the temperature range 100-1200 °C and converted to mole of hydrogen per mole of Ba(Ce_xZr_{10-x})_{0.08}Y_{0.2}O_{3-\delta}, (1 \le x \le 9) oxides. Finally, the effect of buoyancy was corrected using data from a blank test.

4.5 Steam electrolysis cell fabrication and testing

Steam electrolysis cathode-supported electrolyte half-cells were fabricated by sequential tape-casting using a KAROcast 300-7 micro-tape casting device (KMS Automation GmbH Germany). The support layer slurry consisted of commercial NiO powder (Vogler, raw material) and SrZr_{0.5}Ce_{0.4}Y_{0.1}O_{2.95} with a ratio of NiO-SrZr_{0.5}Ce_{0.4}Y_{0.1}O_{2.95} = 60:40 in wt%, dispersed in an ethanol and methyl ethyl ketone (MEK) mixture together with Nuosperse

FX9086 (Elementis Specialties, Inc., London, UK) as the dispersing agent. In addition, polyvinyl butyral (Butvar PVB-98, Solutia Inc., St. Louis, MO, USA), Solusolv 2075 (Solutia Inc., St. Louis, MO, USA), and polyethyleneglycol PEG 400 (Merck Schuchardt, Hohenbrunn, Germany) were added as plasticizers and binder, respectively. The mixture was homogenized in a Thinky ARV310CE planetary mixer and left to rest for about 48 h before casting. Next, the electrolyte layer was cast onto a silicone-coated polymeric (Polyethylene terephthalate) foil. After drying, the cathode functional layer (NiO: SrZr_{0.5}Ce_{0.4}Y_{0.1}O_{2.95} without pore former) was cast on top of the electrolyte (either BaZr_{0.44}Ce_{0.36}Y_{0.2}O_{3-δ} or BaZr_{0.16}Ce_{0.64}Y_{0.2}O_{3-δ}), followed by the substrate supporting layer. The tri-layer tape was then dried and co-sintered at 1500 °C for 10 hours. The sintering profile features ramp rates of 1 °C min⁻¹ and 30 min binder burnouts at 300 and 600 °C and cooling with 2 °C min⁻¹. A Ba_{0.5}La_{0.5}CoO_{3-δ} anode with an effective area of 0.5 cm² was prepared by screen printing the mixture of powder and terpineol (5 wt% ethylcellulose) onto the electrolyte layer and fired at 800 °C/1h. Silver-Palladium pastes and platinum wires were used as current collectors and leads, respectively. Complete cells were mounted and sealed with pyrex glass in a Probostat (NorECS, Oslo, Norway). The anode was supplied with humidified 80 vol. % H₂O mixed and 1vol. % O₂ / 99 vol. %Ar/ (30 mL·min⁻¹) carrier gas. At the same time, $1\%H_2/Ar 99\% (30 \text{ mL} \cdot \text{min}^{-1})$ at the cathode $(P_{H2O} = 1.9 \times 10^3 \text{ Pa})$. A hygrometer chilled mirror (UHQ-4P, Buck Research Instruments LLC, Tokyo, Japan) monitored the anode inlet's water vapor pressure. Gas lines were kept heated at 120 °C to prevent the condensation of water vapor. The hydrogen evolution was determined by measuring the increase in hydrogen concentration in the cathode gas outlet by gas chromatography (Varian CP-4900 micro-Gas Chromatograph equipped with a micro-machined Thermal Conductivity Detector (TCD), Agilent Technologies Inc., Tokyo, Japan). Faradaic efficiencies were obtained based on the experimental hydrogen generation rate and theoretical one at fixed current densities.

Supporting Information

Supporting Information is available from the Wiley Online Library.

Acknowledgments

The authors gratefully acknowledge financial support through JSPS KAKENHI Grant-in-Aid for Scientific Research (C), No. 19K05672, JSPS Core-to-Core Program of Advanced Research Networks (Solid Oxide Interfaces for Faster Ion Transport), NEDO (International collaboration work in the field of clean energy) No: No. 20001458-0, the International Institute for Carbon-Neutral Energy Research (I2CNER) sponsored by the World Premier International Research Center Initiative (WPI), MEXT Japan and the Helmholtz Association of German Research Centres under the POF-MTET program.

The authors declare no conflict of interest.

Received: ((will be filled in by the editorial staff))

Revised: ((will be filled in by the editorial staff))

Published online: ((will be filled in by the editorial staff))

References

[1] S. Choi, T. C. Davenport, S. M. Haile, *Energy and Environmental Science* **2019**, *12*, 206.

[2] H. An, H. W. Lee, B. K. Kim, J. W. Son, K. J. Yoon, H. Kim, D. Shin, H. Il Ji, J. H. Lee, *Nature Energy* **2018**, *3*, 870.

[3] C. Duan, R. Kee, H. Zhu, N. Sullivan, L. Zhu, L. Bian, D. Jennings, R. O'Hayre, Nature Energy 2019, 4, 230.

24

- [4] D. Han, X. Liu, T. S. Bjørheim, T. Uda, Advanced Energy Materials 2021, 11, 1.
- [5] H. Iwahara, T. Esaka, H. Uchida, N. Maeda, Solid State Ionics 1981, 3–4, 359.
- [6] K. Leonard, Y. S. Lee, Y. Okuyama, K. Miyazaki, H. Matsumoto, *International Journal of Hydrogen Energy* **2017**, *42*, 3926.
- [7] Y. Okuyama, T. Kozai, S. Ikeda, M. Matsuka, T. Sakai, H. Matsumoto, *Electrochimica Acta* **2014**, *125*, 443.
- [8] L. Lei, J. Zhang, Z. Yuan, J. Liu, M. Ni, F. Chen, *Advanced Functional Materials* **2019**, *29*, 1.
- [9] K. D. Kreuer, Annual Review of Materials Research 2003, 33, 333.
- [10] A. Manthiram, J. F. Kuo, J. B. Goodenough, Solid State Ionics 1993, 62, 225.
- [11] F. G. Kinyanjui, S. T. Norberg, C. S. Knee, I. Ahmed, S. Hull, L. Buannic, I. Hung, Z. Gan, F. Blanc, C. P. Grey, S. G. Eriksson, *Journal of Materials Chemistry A* **2016**, *4*, 5088.
- [12] K. D. Kreuer, T. Dippel, Y. M. Baikov, J. Maier, Solid State Ionics 1996, 86–88, 613.
- [13] T. Norby, Solid State Ionics 1999, 125, 1.
- [14] W. Wang, A. V. Virkar, *Journal of Power Sources* **2005**, *142*, 1.
- [15] A. W. England, G. Simmons, D. Strangway, *Journal of Geophysical Research* 1968, 73, 3219.
- [16] Y. Yoo, N. Lim, Journal of Power Sources **2013**, 229, 48.
- [17] S. Ricote, N. Bonanos, A. Manerbino, W. G. Coors, *International Journal of Hydrogen Energy* **2012**, *37*, 7954.
- [18] S. M. Babiniec, S. Ricote, N. P. Sullivan, *International Journal of Hydrogen Energy* **2015**, *40*, 9278.
- [19] G. Chiodelli, L. Malavasi, C. Tealdi, S. Barison, M. Battagliarin, L. Doubova, M. Fabrizio, C. Mortalò, R. Gerbasi, *Journal of Alloys and Compounds* **2009**, *470*, 477.
- [20] H. Matsumoto, I. Nomura, S. Okada, T. Ishihara, Solid State Ionics 2008, 179, 1486.

- [21] S. M. Haile, G. Staneff, K. H. Ryu, Journal of Materials Science 2001, 36, 1149.
- [22] A. Grimaud, J. M. Bassat, F. Mauvy, P. Simon, A. Canizares, B. Rousseau, M. Marrony, J. C. Grenier, *Solid State Ionics* 2011, 191, 24.
- [23] D. Han, Y. Noda, T. Onishi, N. Hatada, M. Majima, T. Uda, *International Journal of Hydrogen Energy* **2016**, *41*, 14897.
- [24] K. Katahira, Y. Kohchi, T. Shimura, H. Iwahara, Solid State Ionics 2000, 138, 91.
- [25] K. H. Ryu, S. M. Haile, Solid State Ionics 1999, 125, 355.
- [26] J. Lagaeva, D. Medvedev, A. Demin, P. Tsiakaras, Journal of Power Sources 2015, 278, 436.
- [27] S. Barison, M. Battagliarin, T. Cavallin, L. Doubova, M. Fabrizio, C. Mortalò, S.
 Boldrini, L. Malavasi, R. Gerbasi, *Journal of Materials Chemistry* 2008, 18, 5120.
- [28] R. Murphy, Y. Zhou, L. Zhang, L. Soule, W. Zhang, Y. Chen, M. Liu, *Advanced Functional Materials* **2020**, *30*, 1.
- [29] H. Matsumoto, T. Sakai, Y. Okuyama, Pure and Applied Chemistry 2013, 85, 427.
- [30] Y. Okuyama, K. Isa, Y. S. Lee, T. Sakai, H. Matsumoto, *Solid State Ionics* **2015**, *275*, 35.
- [31] Y. Takamura, K. Leonard, A. Luo, L. W. Martin, H. Matsumoto, *Journal of Solid State Electrochemistry* **2019**, *23*, DOI 10.1007/s10008-018-04188-z.
- [32] T. Fujisaki, A. T. Staykov, Y. Jing, K. Leonard, N. R. Aluru, H. Matsumoto, *Solid State Ionics* 2019, 333, DOI 10.1016/j.ssi.2019.01.009.
- [33] S. Maeda, Y. Shiratori, D. Kurashina, T. Fujisaki, K. Leonard, H. Matsumoto, International Journal of Hydrogen Energy 2020, 45, 4026.
- [34] E. Fabbri, A. D'Epifanio, E. Di Bartolomeo, S. Licoccia, E. Traversa, *Solid State Ionics*2008, 179, 558.
- [35] R. D. Shannon, Acta Cryst. **1976**, A32, 751.
- [36] T. Pagnier, I. Charrier-Cougoulic, C. Ritter, G. Lucazeau, Eur. Phys. J. AP 2000, 9, 1.

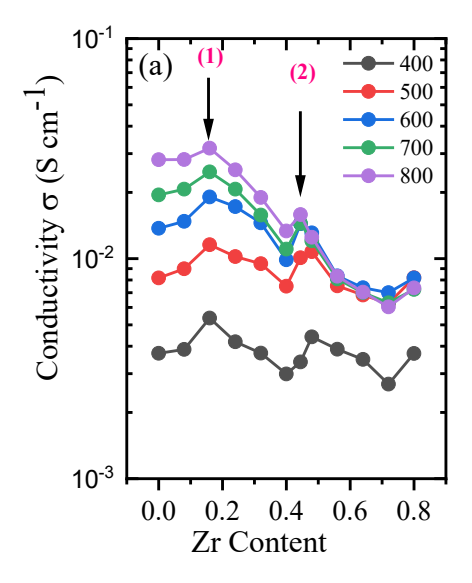
- [37] C. Zuo, S. Zha, M. Liu, M. Hatano, M. Uchiyama, Advanced Materials 2006, 18, 3318.
- [38] L. Yang, S. Wang, K. Blinn, M. Liu, Z. Liu, Z. Cheng, M. Liu, *Science* **2009**, *326*, 126.
- [39] S. Choi, C. J. Kucharczyk, Y. Liang, X. Zhang, I. Takeuchi, H. Il Ji, S. M. Haile, Nature Energy 2018, 3, 202.
- [40] Y. Okuyama, T. Kozai, T. Sakai, M. Matsuka, H. Matsumoto, *Electrochimica Acta* **2013**, *95*, 54.
- [41] D. Shima, S. M. Haile, Solid State Ionics 1997, 97, 443.
- [42] A. Løken, T. S. Bjørheim, R. Haugsrud, *Journal of Materials Chemistry A* **2015**, *3*, 23289.
- [43] T. Somekawa, Y. Matsuzaki, M. Sugahara, Y. Tachikawa, H. Matsumoto, S. Taniguchi, K. Sasaki, *International Journal of Hydrogen Energy* **2017**, *42*, 16722.
- [44] Y. Yamazaki, P. Babilo, S. M. Haile, Chemistry of Materials 2008, 20, 6352.
- [45] D. K. Lim, H. N. Im, S. J. Song, H. I. Yoo, Scientific Reports 2017, 7, 1.
- [46] T. Norby, M. Widerøe, R. Glöckner, Y. Larring, Dalton Transactions 2004, 3012.
- [47] T. S. Bjørheim, A. Kuwabara, I. Ahmed, R. Haugsrud, S. Stølen, T. Norby, *Solid State Ionics* **2010**, *181*, 130.
- [48] T. S. Bjørheim, A. Løken, R. Haugsrud, *Journal of Materials Chemistry A* **2016**, *4*, 5917.
- [49] T. Chen, Y. Jing, L. O. Anderson, K. Leonard, H. Matsumoto, N. Aluru, N. H. Perry, The Journal of Physical Chemistry C 2021, DOI 10.1021/acs.jpcc.1c08334.
- [50] R. Sažinas, M. F. Sunding, A. Thøgersen, I. Sakaguchi, T. Norby, T. Grande, J. M. Polfus, *Journal of Materials Chemistry A* 2019, 7, 3848.
- [51] R. Sažinas, C. Bernuy-López, M. A. Einarsrud, T. Grande, *Journal of the American Ceramic Society* **2016**, *99*, 3685.
- [52] K. Leonard, W. Deibert, M. E. Ivanova, W. A. Meulenberg, T. Ishihara, H. Matsumoto, *Membranes* **2020**, *10*, 1.

- [53] M. E. Ivanova, S. Escolástico, M. Balaguer, J. Palisaitis, Y. J. Sohn, W. A. Meulenberg, O. Guillon, J. Mayer, J. M. Serra, *Scientific Reports* 2016, 6, 1.
- [54] W. Deibert, M. E. Ivanova, Y. Huang, R. Merkle, J. Maier, W. A. Meulenberg, *Journal of Materials Chemistry A* **2021**, *00*, 1.
- [55] J. Kim, A. Jun, O. Gwon, S. Yoo, M. Liu, J. Shin, T. H. Lim, G. Kim, *Nano Energy*2018, 44, 121.
- [56] T. Kobayashi, K. Kuroda, S. Jeong, H. Kwon, C. Zhu, H. Habazaki, Y. Aoki, *Journal of The Electrochemical Society* **2018**, *165*, F342.
- [57] F. He, D. Song, R. Peng, G. Meng, S. Yang, *Journal of Power Sources* **2010**, *195*, 3359.
- [58] J. Lyagaeva, N. Danilov, G. Vdovin, J. Bu, D. Medvedev, A. Demin, P. Tsiakaras, *Journal of Materials Chemistry A* **2016**, *4*, 15390.
- [59] M. A. Azimova, S. McIntosh, *Solid State Ionics* **2011**, *203*, 57.
- [60] D. Huan, N. Shi, L. Zhang, W. Tan, Y. Xie, W. Wang, C. Xia, R. Peng, Y. Lu, ACS Applied Materials and Interfaces 2018, 10, 1761.
- [61] K. Leonard, J. Druce, V. Thoreton, J. A. Kilner, H. Matsumoto, *Solid State Ionics*2018, 319, 218.
- [62] K. Leonard, Y. Okuyama, Y. Takamura, Y. S. Lee, K. Miyazaki, M. E. Ivanova, W. A. Meulenberg, H. Matsumoto, *Journal of Materials Chemistry A* **2018**, *6*, 19113.

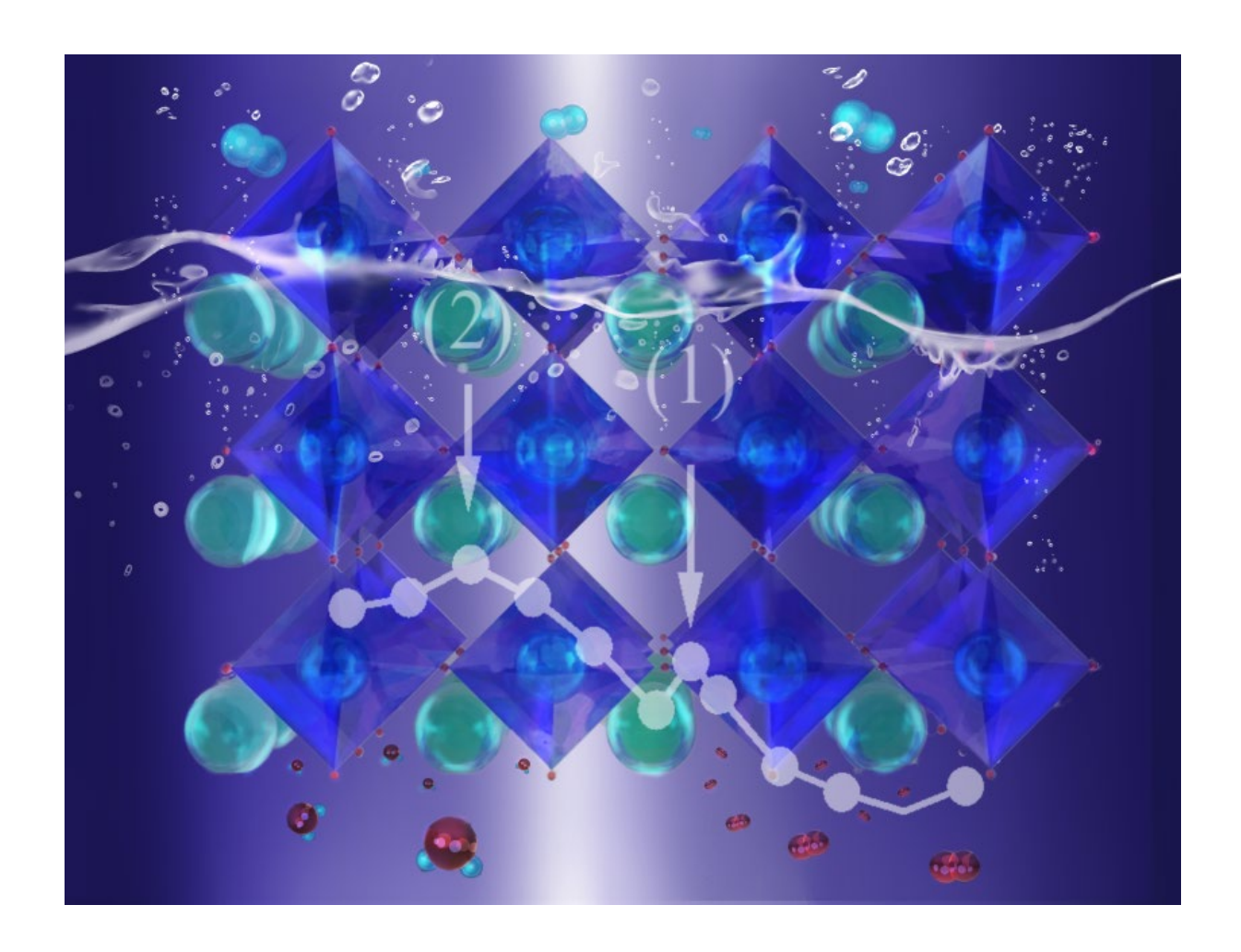


Tailored and improved protonic conductivity through Ba(Z_xCe_{10-x})0.08 $Y_{0.2}O_{3-\delta}$ ceramics perovskites type oxides for electrochemical devices

ToC figure



We report two new variants in the $Ba(Zr_xCe_{10-x})_{0.08}Y_{0.2}O_{3-\delta}$, family achieved by fixing a cerium/zirconium ratio of 5:4 at the perovskite B-site. The oxides exemplified by $BaZr_{0.44}Ce_{0.36}Y_{0.2}O_{3-\delta}$ and $BaZr_{0.16}Ce_{0.64}Y_{0.2}O_{3-\delta}$, exhibiting high conductivity (10.1 and 11.5 mS cm⁻¹ at 500 °C) allow successful hydrogen production in a steam electrolyzer prototype



The cover image illustrates a new composition variant in the $Ba(Zr_xCe_{1-x})Y_yO_{3-\delta}$ family achieved by fixing a cerium/zirconium ratio of 5:4 at the perovskite B-site. The said composition $BaZr_{0.44}Ce_{0.36}Y_{0.2}O_{3-\delta}$ demonstrates a superior ionic conductivity (10.1 mS cm⁻¹ at 500 °C) to stability trade-off than some of the current state-of-the-art ceramic proton-conducting electrolytes. More information can be found in the Research Article by K. Leonard et al......